Title

Development of methods and feasibility of using hyperpolarized carbon-13 imaging data for evaluating brain metabolism in patient studies

Authors

Park, Ilwoo
Larson, Peder EZ
Gordon, Jeremy W
et al.

Development of Methods and Feasibility of Using Hyperpolarized Carbon-13 Imaging Data for Evaluating Brain Metabolism in Patient Studies

Ilwoo Park,[1] Peder E.Z. Larson ⓘ,[2] Jeremy W. Gordon,[2] Lucas Carvajal,[2] Hsin-Yu Chen,[2] Robert Bok,[2] Mark Van Criekinge,[2] Marcus Ferrone,[3] James B. Slater,[2] Duan Xu,[2] John Kurhanewicz,[2] Daniel B. Vigneron,[2,4] Susan Chang,[5] and Sarah J. Nelson[2,4]*

Purpose: Hyperpolarized carbon-13 (^{13}C) metabolic imaging is a noninvasive imaging modality for evaluating real-time metabolism. The purpose of this study was to develop and implement experimental strategies for using [1-^{13}C]pyruvate to probe in vivo metabolism for patients with brain tumors and other neurological diseases.
Methods: The ^{13}C radiofrequency coils and pulse sequences were tested in a phantom and were performed using a 3 Tesla whole-body scanner. Samples of [1-^{13}C]pyruvate were polarized using a SPINlab system. Dynamic ^{13}C data were acquired from 8 patients previously diagnosed with brain tumors, who had received treatment and were being followed with serial magnetic resonance scans.
Results: The phantom studies produced good-quality spectra with a reduction in signal intensity in the center attributed to the reception profiles of the ^{13}C receive coils. Dynamic data obtained from a 3-cm slice through a patient's brain following injection with [1-^{13}C]pyruvate showed the anticipated arrival of the agent, its conversion to lactate and bicarbonate, and subsequent reduction in signal intensity. A similar temporal pattern was observed in 2D dynamic patient studies, with signals corresponding to pyruvate, lactate, and bicarbonate being in normal appearing brain, but only pyruvate and lactate being detected in regions corresponding to the anatomical lesion. Physiological monitoring and follow-up confirmed that there were no adverse events associated with the injection.
Conclusion: This study has presented the first application of hyperpolarized ^{13}C metabolic imaging in patients with brain tumor and demonstrated the safety and feasibility of using hyperpolarized [1-^{13}C]pyruvate to evaluate in vivo brain metabolism. **Magn Reson Med 000:000–000, 2018. © 2018 International Society for Magnetic Resonance in Medicine.**

INTRODUCTION

Hyperpolarized carbon-13 (^{13}C) magnetic resonance (MR) metabolic imaging is a nonionizing, nonradioactive imaging method that can be used to measure real-time metabolism. The recent development of dissolution dynamic nuclear polarization (DNP) offers an exciting method for assessing in vivo metabolism, with a huge gain in signal intensity over the conventional ^{13}C MR methods (1) and enables the acquisition of ^{13}C metabolic imaging data with high spatial resolution in a short time (2). One of the first applications of this technology has been to evaluate the conversion of [1-^{13}C]pyruvate to [1-^{13}C]lactate. This is particularly relevant for monitoring tumor growth and assessing response to therapy because malignant cells frequently have upregulated lactate dehydrogenase A, which is the enzyme that regulates this pathway (3,4). Preclinical studies that have shown promising results include the assessment of a wide range of different cancers, as well as cardiac disease, traumatic brain injury, and multiple sclerosis (5–13).

The first-in-human study using hyperpolarized ^{13}C metabolic imaging was performed in patients with prostate cancer and was able to demonstrate the safety and feasibility of the technology in a clinical setting (14). This has led to great interest in applying similar methods to other groups of patients and also for volunteer cardiac studies (15). The purpose of the current study was to develop and implement hyperpolarized ^{13}C metabolic imaging using [1-^{13}C]pyruvate in the human brain, with the long-term goal of being able to monitor in vivo metabolism for patients with brain tumors and other neurological diseases. The ^{13}C coils and pulse sequences designed for this application were first tested in phantoms. Dynamic ^{13}C data were then obtained from patients with a prior diagnosis of glioma, which is the most common primary brain tumor in adults.

[1]Department of Radiology, Chonnam National University Medical School and Hospital, Gwangju, Korea.
[2]Department of Radiology and Biomedical Imaging, University of California, San Francisco, California, USA.
[3]Department of Clinical Pharmacy, University of California, San Francisco, California, USA.
[4]Department of Bioengineering and Therapeutic Sciences, University of California, San Francisco, California, USA.
[5]Department of Neurological Surgery, University of California, San Francisco, California, USA.

*Correspondence to: Sarah J. Nelson, Ph.D., University of California, 1700 4th Street, Box 2532, BH-303, San Francisco, CA 94158, USA.
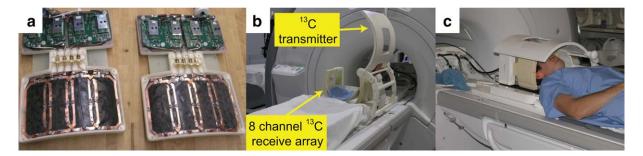E-mail: Sarah.Nelson@ucsf.edu

FIG. 1. ^{13}C RF coil configurations developed for human brain study. (a) Eight-channel ^{13}C phased-array coils. (b) Clamshell volumetric ^{13}C transmit coil and bilateral eight-channel phased-array receive coils. (c) A picture of ^{13}C RF coil setup with a volunteer.

METHODS

^{13}C MR setup

All experiments were performed using a 3 Tesla (T) clinical magnetic resonance imaging (MRI) system (GE Healthcare, Waukesha, WI) with 50-mT/m, 200-mT/m/ms gradients and a multinuclear spectroscopy hardware package. The ^{13}C radiofrequency (RF) coil configuration comprised a bore-insertable ^{13}C volume coil for transmission (16) and a bilateral eight-channel phased-array coil for reception (17) (Fig. 1a,b). The standard patient headrest holder was modified so that the subjects were comfortably stabilized in the ^{13}C RF coil setup, whereas the two phased-array receive coils were placed around the head (Fig. 1c).

^{13}C coil loading tests

To investigate the effect of coil loading on the ^{13}C signal, a B_1+ map was acquired using the double-angle method (18) in both unloaded and loaded scenarios using a head-shaped phantom containing unenriched ethylene glycol ($HOCH_2CH_2OH$, anhydrous, 99.8%; Sigma-Aldrich, St. Louis, MO). To acquire the B_1+ map, a single-band spectral-spatial RF pulse (full width at half maximum = 120 Hz) was used to selectively excite the central ^{13}C resonance of ethylene glycol and avoid artifacts arising from chemical shift, and then encoded with a single-shot symmetric echo-planar readout (19). The total readout duration was 15.46 ms (24 echoes, 0.644 ms echo spacing), with $\alpha = 30°$, $2\alpha = 60°$, and 100 averages (7.5×7.5 mm in-plane resolution, 24×24 cm field of view [FOV], 32×32 matrix, 10-cm slice thickness, and repetition time [TR]/echo time [TE] = 3,000/15.6 ms; the total scan time was 10 minutes). The B_1 map was acquired unloaded (with just the head phantom) and loaded (with the head phantom plus saline). Loading was confirmed with a change from –7 to –11 dB using a network analyzer. The flip angles over the ethylene glycol phantom were assessed as grayscale maps and histograms and compared between the loaded and unloaded cases.

Phantom tests

The phantom was scanned using the clamshell/phased array coil configuration shown in Figure 1. For these scans, the distance between the center of the two receive coils was 17 cm. ^{13}C spectral data were acquired from a 2-cm slice using a dynamic ^{13}C 2D echo-planar spectroscopic imaging (EPSI) sequence with TR/TE = 3,000/6.1 ms, 20×20 mm^2 nominal in-plane resolution (20), 10 phase encodes in the right-left (RL) direction, and a symmetric echo-planar readout in the anteroposterior (AP) direction with a constant 90° flip angle excitation.

Patient population

Eight patients who had a prior diagnosis of glioma were recruited from the neuro-oncology clinic at our institution. Table 1 summarizes their clinical parameters. They had all received multiple treatments and were being

Table 1
Patient Characteristics and QC Values for the ^{13}C Injections

Patient no.	Sex	Weight (kg)	Initial diagnosis age (years)	Time to scan (years)[a]	Current diagnosis	Subsequent clinical status	EPA conc (µM)	pyr conc (nM)	% polariz-ation	pH	Time to injection (sec)
1	M	81.4	35	19	OD2	Stable	0.50	247	33	7.3	81
2	M	73.5	30	8	GBM	Progressed	1.40	236	38	7.5	84
3	M	75.8	38	6	OD2	Reop/AA	0.30	223	39	8.1	114
4	M	93.0	25	12	AA	Reop/AA	3.00	221	43	7.8	86
5	F	81.2	58	2	GBM	Progressed	1.30	249	43	7.0	96
6	M	99.4	36	12	OD3	Stable	0.90	239	32	7.4	85
7	F	65.0	46	2	GBM	Reop/TE	0.20	232	33	7.9	74
8	F	78.0	54	1	GBM	Stable	0.30	242	35	7.2	87

[a]Time from initial diagnosis to the ^{13}C scan.
OD2, oligodendroglioma grade 2; OD3, oligodendroglioma grade 3; AA, anaplastic astrocytoma (grade 3); GBM, glioblastoma (grade 4); TE, treatment effect; EPA, electron paramagnetic agent.

Table 2
Summary of the Acquisition Parameters for the Patient ^{13}C Data, as Well as the Time Point and SNR for Maximum Pyruvate and Lactate

Patient no.	Scan type[a]	Flip angle (°)	No. of time points	Voxel size (RL × AP × SI cm)	Matrix size[b]	Peak time point (s)		Delay	Maximum SNR	
						pyr	lac	Δt (s)	pyr	lac
1	Slice-select	10	40	3 cm slice	—	15	24	9	3,266	293
2	2D EPSI	10	24	2 × 2 × 2	10 × 18	6	15	9	754	103
3	2D EPSI	10	24	2 × 2 × 2	10 × 18	9	18	9	286	38
4	2D EPSI	10	16	2 × 2 × 2	10 × 18	3	12	9	665	53
5	2D EPSI	10	24	1.8 × 1.8 × 2	10 × 18	3	12	9	714	38
6	2D EPSI	10	24	1.5 × 1.5 × 2	12 × 18	3	12	9	388	25
7	2D EPSI-mb	Variable	10	2 × 2 × 3	10 × 18	6	12	6	119	83
8	2D EPSI-mb	Variable	10	2 × 2 × 2	10 × 18	3	12	9	169	91

All studies were acquired with a temporal resolution of 3 seconds. lac and pyr represent lactate and pyruvate, respectively.
[a]Slice-select, 2D EPSI, and 2D EPSI-mb represent slice-selective dynamic, 2D-localized dynamic echo-planar spectroscopic imaging, and multiband RF 2D-localized dynamic echo-planar spectroscopic imaging pulse sequence, respectively.
[b]Matrix size in phase encode (RL) × EPSI (AP) directions.

followed with MRI. An Investigational New Drug (IND) had been obtained from the U.S. Food and Drug Administration for generating the agent and implementing the clinical protocol. Patients provided written informed consent for participation in the study, which had institutional review board approval. Electrocardiogram monitoring was performed at baseline and within 1 hour after the pyruvate injection. Clinical follow-up assessments were performed at 24 hours.

Sample formulation and polarization

For patients scans, the hyperpolarized [1-^{13}C]pyruvate was produced using a SPINlab (General Electric, Niskayuna, NY) DNP polarizer that is adjacent to the 3T MR scanner. The pharmacy kit (fluid path) was filled in an ISO 5 environment utilizing an isolator (Getinge Group, Getinge, France) and a clean bench laminar flow hood. The mixture used for polarization comprised 1.432 g of [1-^{13}C]pyruvic acid (MilliporeSigma, Miamisburg, OH) and 28 mg of trityl radical (GE Healthcare, Oslo, Norway). The fluid path was then loaded into one of the available channels in the SPINlab polarizer. After approximately 2.5 hours of microwave irradiation at 140 GHz, the mixture of [1-^{13}C]pyruvic acid and trityl radical was dissolved in sterile water and forced through a filter that removed trityl radical to a level below 3 μM. The solution was then collected in a receiver vessel, neutralized, and diluted with a sodium hydroxide tris(hydroxymethyl)aminomethane/ethylenediaminetetraacetic acid buffer solution. The receive assembly that accommodates quality-control (QC) processes provided rapid measurements of pH, temperature, residual electron paramagnetic agent (EPA) concentration, volume, pyruvate concentration, and polarization level. The final step in the automated compounding procedure was for the drug product to be passed through a sterilizing filter (0.2 μm; ZenPure, Manassas, VA) within the SPINlab QC system immediately before being collected in a sterile Medrad syringe.

Once the preparation was complete, a sterile filter integrity test was performed in parallel with the pyruvate solution being transported to the MRI scan room and being set up on a power injector. Successful QC and filter integrity tests were required before the hyperpolarized pyruvate doses were released for patient injections. The acceptance criteria for the hyperpolarized pyruvate injection were: 1) polarization > =15%; 2) pyruvate concentration between 220 and 280 mM; 3) EPA concentration < =3.0 μM; 4) pH between 5.0 and 9.0; 5) temperature between 25.0 and 37.0 °C; 6) volume > 38 mL; and 7) filter integrity passes the bubble point test at 50 psi. Following approval from the pharmacist, a sample corresponding to a dose of 0.43 mL/kg from the approximately 250-mM pyruvate solution was delivered to the subject at a rate of 5 mL/s. After completion of pyruvate injection, a further 20 mL of sterile saline was injected at a rate of 5 mL/s. The polarization, QC, and timing parameters are summarized in Table 1.

Imaging protocol for patient study

Before the start of each examination, patients were monitored to establish their baseline vital signs and an intravenous catheter was placed in their antecubital vein. After positioning in the scanner with the ^{13}C coil setup covering as much of the lesion as possible, T_2-weighted fast spin echo images (TR/TE = 60/4,000 ms, 26-cm FOV, 192 × 256 matrix, 5-mm slice thickness, and number of excitations = 2) were acquired with the ^{1}H body coil to provide an anatomical reference. Frequency calibration was performed with the ^{13}C coils using the sealed standard that is housed within one of the eight-channel phased array elements and contains 1 mL of 8 M of ^{13}C-urea. Once the appropriate scan parameters had been defined, the operators of the SPINlab system started the dissolution process. When the pharmacist had approved the results provided by the QC system and filter integrity tests, the pyruvate solution and saline flush were administered into the patient. Dynamic ^{13}C data were acquired starting 5 seconds after the end of the saline injection from an axial slab that was centered over the anatomical lesion.

The acquisition parameters for the ^{13}C data are summarized in Table 2. For patient 1, the dynamic data were acquired from a 30-mm axial slice with a 10° flip angle, TR/TE = 3,000/35 ms, 3-second temporal resolution, and 40 total time points. For 5 patients, 2D-localized

dynamic EPSI data were obtained from a 20-mm axial slice with a constant $10°$ flip angle, 24 total time points, either 10 or 12 phase encodes in the RL direction, and a symmetric echo-planar readout in the AP direction (20). The TR/TE was 130/6.1 ms, the time resolution was 3 seconds, and the nominal in-plane spatial resolution was either 15×15, 18×18, or 20×20 mm^2 (21). The EPSI readout contained the following parameters: spectral resolution $= 10.4$ Hz, EPSI duration $= 96.4$ ms, spectral bandwidth $= 543$ Hz, minimum resolution $= 4.8$ mm, signal-to-noise ratio (SNR) efficiency $= 0.94$. Similar dynamic EPSI data were obtained for the other 2 patients, but with an excitation scheme that utilized a multiband RF pulse and progressively increasing flip angle scheme (22,23). These flip angle schemes were designed to efficiently use the magnetization in several ways: use lower flip angles on pyruvate to increase the magnetization available for metabolic conversion, evenly distribute magnetization throughout the acquisition by accounting for T_1 decay, prior RF excitations, and metabolic conversion; and use all available magnetization by the end of the experiment (23). The plot of pyruvate, lactate, and bicarbonate flip angles across all excitations are shown in Supporting Figure S1. At the completion of the ^{13}C examination, patients were taken out of the scanner for postinjection monitoring and then brought back for a subsequent standard ^{1}H MR examination that was obtained with a conventional head coil.

Data analysis

The slice-localized dynamic ^{13}C data were processed with MATLAB (version 7.0; The MathWorks, Inc., Natick, MA). Individual free induction decays were apodized with a 10-Hz Gaussian filter in the time domain and Fourier-transformed to produce ^{13}C spectra at each time point. The 2D EPSI dynamic ^{13}C data were processed with software developed in our laboratory including the Spectroscopic Image Visualization and Computing (SIVIC) package (24,25). The odd and even echoes of the symmetric EPSI readout were separated and processed by the following steps: 1) apodization by a 10-Hz Gaussian filter in the time domain; 2) correction of timing delays between spatial k-space samples; 3) ramp samples were gridding onto a uniform grid; 4) Fourier-transformed; and 5) combined with linear phase added to correct for timing differences between the even and odd data. This produced a time series of spectroscopic imaging data for each coil element. In order to correct for the aliased bicarbonate chemical shift, the second set of data were generated by demodulating the raw data at a different frequency before reconstruction. The coil combination algorithm used for the slice select and initial review of the 2D EPSI data utilized a magnitude sum of squares algorithm. Subsequent quantitative analysis of the 2D EPSI data utilized a linear combination of phase-sensitive spectra from different receive coils with phases and weights determined from the intensity of the pyruvate signal from the time point at which it was at a maximum. In addition to the dynamic analysis, a single spectral array was calculated by summing the time series on a voxel-by-voxel basis. Peak

intensities for lactate and pyruvate were estimated from the spectral array that was reconstructed at the original reference frequency, and the peak intensities for bicarbonate were estimated from the array that was reconstructed at its frequency. To perform this analysis, each array was baseline subtracted, then frequency and phase corrected using methods described previously for H-1 data (25). SNRs were calculated as the peak height over the standard deviation from regions in the spectra without any metabolic signal.

To relate the ^{13}C data with anatomical features, the fluid attenuation inversion recovery (FLAIR) and T_1-weighted post-Gd (gadolinium) images obtained from the subsequent ^{1}H imaging examination were aligned with the body-coil T_2-weighted images. A mask corresponding to brain parenchyma was obtained using the FSL brain extraction tool. The T_2 lesion was defined using manual segmentation. This was then subtracted from the mask of brain parenchyma in order to unambiguously define regions of normal-appearing brain (NAB) tissue. The following criteria were used to classify the voxels for NAB or T_2 lesion: 1) Voxels from NAB were defined as being at least 80% within the brain, having no overlap with the T_2 lesion, and having lactate SNR greater than 10.0 and bicarbonate SNR greater than 5.0; 2) for the T_2 lesion, the voxels that were overlapped by more than 30% with the T_2 lesion and had lactate SNR greater than 10.0 were chosen.

RESULTS

^{13}C coil loading test

Figure 2A shows the results from the ^{13}C coil loading test. The B_1+ field measured using the double-flip-angle method (26) appeared to be similar between the unloaded and loaded conditions. The calculated flip angles from the flip angle maps and histograms were $28° \pm 7°$ (n = 3) and $26° \pm 8°$ (n = 3) for the unloaded and loaded condition, respectively. This meant that the power requirements did not change between the loaded and unloaded conditions, and a power calibration on the head phantom could be used for patient studies. Based on these results, the ethylene glycol phantom shown was used to calibrate the transmit gain for the ^{13}C sequence before subjects were placed on the scanner.

Phantom data

The ^{13}C coils and sequences detected ^{13}C signal from the phantom (Fig. 2b), but with 3- to 4-fold lower intensity in the center of the FOV attributed to the reception profiles of the receive coil elements. This is in agreement with previous tests done in a study that focused on evaluating data from the brain of a nonhuman primate (21).

Patient data

All patients tolerated the pyruvate injection well, and no adverse effects were observed or reported subsequently. Levels of polarization and QC parameters obtained are presented in Table 1 and were well within the specifications defined in the IND. The mean EPA concentration
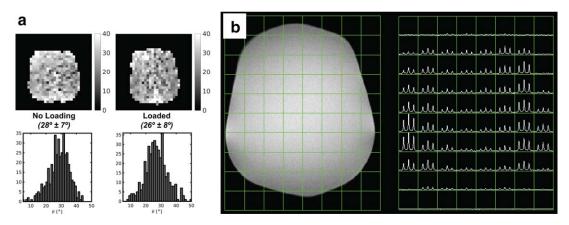
FIG. 2. Results from the ^{13}C coil loading and initial data acquisition tests. (a) B$_1$ + maps of flip angle were calculated using a double-flip-angle method and showed that the B1 maps were similar between the unloaded and loaded conditions. (b) 2D EPSI data from the head-shaped phantom containing ethylene glycol demonstrated the combined reception profile of the receive coils.

was 0.99 μM (range, 0.2–3.0), pyruvate concentration was 236 mM (range, 221–249), polarization was 37% (range, 32–43), and pH was 7.5 (range, 7.0–8.1). The mean scan start time measured from the start of dissolution was 88 seconds (range, 74–114).

Figure 3 shows the slice-localized ^{13}C dynamic data from a 30-mm-thick axial slice for subject 1. The location of the slice is defined on the sagittal image in Figure 3A. The ^{13}C dynamic spectra are represented as a stack plot in Figure 3B. They are displayed in magnitude mode and were acquired with a time resolution of 3 seconds. SNRs of pyruvate, lactate, and bicarbonate are plotted as a function of time in Figure 3c. The pyruvate signal at 173 parts per million (ppm) reached a maximum with SNR of 3,266 at approximately 15 seconds from the start of the data acquisition, whereas the lactate signal at 185 ppm reached a maximum SNR of 293 at 24 seconds, which was 9 seconds later. The pyruvate signal decreased rapidly from the maximum peak. Pyruvate-hydrate was observed as a peak lying between the pyruvate and lactate resonances, but had relatively low signal amplitude (Fig. 3b). Signal from bicarbonate was detected at approximately 162 ppm and had lower intensity than lactate (Fig. 3c).

The peak time point and maximum voxel SNR for the 2D EPSI dynamic data are shown in Table 2. Although the time at which the pyruvate delivery was a maximum varied from 3 to 9 seconds, the additional delay for reaching the highest lactate was 9 seconds for 6 of the 7 patients and 6 seconds for 1 patient. As expected, the maximum SNRs was lowest for patient 3, for whom the time to injection was the longest at 114 seconds, and the second lowest for patient 6, for whom the number of phase encodes was increased and the voxel resolution reduced. The maximum SNR for pyruvate was lower in patients 7 and 8 because of the multiband excitation and flip angle scheme that was used, but this scheme resulted in higher levels of lactate and bicarbonate. Taken as a whole, these results confirmed that hyperpolarized pyruvate was able to cross the blood–brain barrier and was converted to lactate with a similar time course between subjects.

The acquisition of the 2D EPSI dynamic ^{13}C metabolic imaging data made it possible to investigate spatial variations in metabolism. Figure 4 shows reference anatomical images and spectra from multiple time points for voxels in the T$_2$ lesion (black box) and voxels from contralateral brain tissue (white box) for patient 2. The
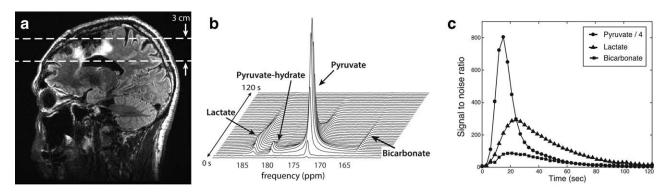

FIG. 3. Slice-localized hyperpolarized ^{13}C dynamic data from patient 1. (a) T$_2$ FLAIR image in a sagittal plane shows the hyperintense region around the resection cavity and the ventricle. (b) The stack plot of ^{13}C magnitude spectra, showing a temporal evolution of lactate, pyruvate, and bicarbonate signal from the brain. (c) The SNR of lactate, pyruvate, urea, and bicarbonate are plotted over time. The pyruvate SNR was divided by 4 so that it could be viewed on the same graph as the pyruvate and bicarbonate.
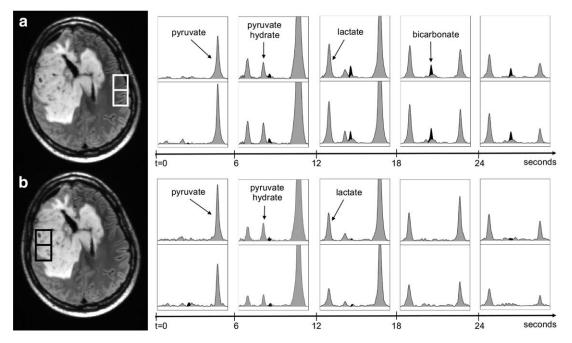
FIG. 4. Temporal changes in spectra from the highlighted voxels in (a) NAB and (b) the T_2 lesion from patient 2. The spectra with peaks shaded in gray are from the data reconstructed at the acquired reference frequency, and the peaks shaded in black represent the data reconstructed at the bicarbonate frequency. The spectra shown are from time at 0, 6, 12, 18, and 24 seconds from the start of data acquisition. The highest pyruvate and pyruvate-hydrate occur at 6 seconds, whereas the highest lactate occurs at time point 15 seconds. It can be seen that there are lactate and bicarbonate peaks in NAB and lactate peaks in the T_2 lesion during the period of 9 to 24 seconds. The chemical shift range is 186.46 to 169.61ppm for all spectroscopic voxels. The intensity scales are arbitrary, but were kept the same for all spectra.

voxels from the T_2 lesion show peaks from lactate, pyruvate-hydrate, and pyruvate, whereas the voxels from contralateral NAB have peaks from lactate, pyruvate-hydrate, bicarbonate, and pyruvate. Note that because of the reduced spectral bandwidth with EPSI, the bicarbonate peak wrapped into a location between pyruvate-hydrate and pyruvate peaks ($\sim$179 ppm). In both cases, lactate peaks were relatively high in the time period between 12 and 24 seconds after the start of data acquisition. The spectra in Figure 5 are from voxels in NAB for patients 3 to 6 at time points where the lactate was highest. Although it is difficult to compare intensities because of variations in the reception profile of the coil, it can be seen that the relative levels of lactate and pyruvate were similar to those for patient 2, but that the bicarbonate peak is absent for the spectrum from patient 6. This may be attributed to the smaller voxel size and the use of 12 rather than 10 phase encodes for data acquisition.

Table 3 shows metabolite intensities and ratios for spectra from patients 2 to 8 that were summed over all time points. In all cases, the maximum lactate and bicarbonate SNRs were higher in the NAB than in the T_2 lesion. Of particular interest is that the 2 patients whose data were acquired with the multiband variable flip angle excitation scheme (patients 7 and 8) have much higher maximum SNR for bicarbonate in NAB (28.8 and 34.1) than patients 2 to 6, but, even in this case, the maximum SNR of bicarbonate from the T_2 lesion was close to or lower than the level considered to be detectable (4.0 and 5.4). The maximum SNR of lactate in the

T_2 lesion was variable between patients, which reflects not only differences in its location relative to the sensitivity profile of the RF coils, but also was attributed to differing contributions from tumor versus treatment effects. The mean lactate/pyruvate for voxels in NAB that had sufficient SNR to provide good estimates of metabolite levels for patients 2 to 6 ranged from 0.18 to 0.38, whereas for patients 7 and 8 they were 0.98 and 0.84. The corresponding values for bicarbonate/pyruvate were 0.06 to 0.15 versus 0.32 and 0.37. The increased metabolite ratios in patients 7 and 8 are likely a result of the multiband variable flip angle scheme used only in these patients.

Figure 6 shows a T_1 post-Gd image, maps of pyruvate, lactate, and bicarbonate SNR, and spectral arrays that were summed over all time points for patient 2. The low signal in the center of the brain is attributed to both the coil reception profile and the lower tissue content on voxels overlapping with the ventricles.

Figure 7 illustrates representative data from patient 2 and patient 8, showing anatomical images as well as color overlays of lactate/pyruvate and bicarbonate/pyruvate on the post-Gd T_1-weighted anatomical images. Despite the differences in acquisition parameters and ratio values, both data sets showed substantial conversion of pyruvate to lactate in NAB and a lack of bicarbonate in the T_2 lesion. Patient 2 had lactate/pyruvate in the T_2 lesion with mean value of 0.30 compared with 0.38 in their NAB, whereas patient 8 had mean lactate/pyruvate of 0.41 within the T_2 lesion compared with 0.84 in their NAB.
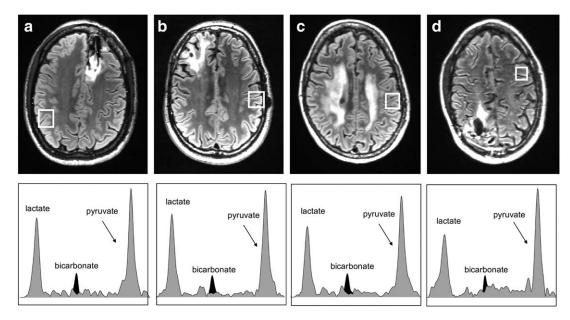
FIG. 5. FLAIR images and spectra in the highlighted NAB voxels at time with maximum lactate from (a) patient 3, (b) patient 4, (c) patient 5, and (d) patient 6. The spectra with peaks shaded in gray are from the data reconstructed at the acquired reference frequency and the peaks shaded in black represent the data reconstructed at the bicarbonate frequency. The relative levels of pyruvate are similar, but the lactate is slightly lower in all patients shown and the bicarbonate is not detectable for patient 6, for whom the acquisition had the smallest voxel size $1.5 \times 1.5 \times 2$ cm and 12 rather than 10 phase encodes. The chemical shift range is 186.46 to 169.61 ppm for all spectroscopic voxels. The intensity scales are arbitrary and were manually set to have similar pyruvate intensity levels between subjects.

DISCUSSION

This study demonstrated the safety and feasibility of using hyperpolarized ^{13}C metabolic imaging for measuring real-time metabolism in the human brain utilizing pyruvate that is transported across the blood–brain barrier by monocarboxylic transporter MCT_1 (27). The slice-localized and 2D EPSI pulse sequences and ^{13}C coils were first tested in a head-shaped phantom. The spatial variation in signal intensity that was observed in the phantom data demonstrated the anticipated variation due to the reception profile of the 2 four-channel paddle array coils, with a 3- to 4-fold reduction in intensity in the center of the phantom versus voxels within 2 to 4 cm of the lateral edges. The focus of these first patient studies was to determine the safety and feasibility. Another focus of the initial study was to define the time course of delivery and metabolism of hyperpolarized [1-^{13}C]pyruvate in both the anatomical lesion and normal appearing brain, as opposed to seeking information about potential diagnostic capabilities at this early stage.

The SPINlab polarizer and the associated QC system provided pyruvate solution with an appropriate pH, temperature, EPA concentration, and polarization level. The average polarization was of 37% which was approximately 2-fold higher than prior polarizations achieved using pre-clinical polarizers (12). This can be explained by the low sample vial temperature in the SPINlab (approximately 0.8 K) compared to the preclinical system (approximately 1.35 K) (28) and its higher magnetic field (5T as opposed to 3.35T). Although the dissolution and

Table 3
Maximum SNR of Metabolites From the Summed Spectra and Ratios of Lactate/Pyruvate and Bicarbonate/Pyruvate

Patient no.	Max SNR: NAB		Max SNR: T$_2$ lesion			Mean ratios: NAB				Mean ratios: T$_2$ lesion			
	lac	bicarb	lac	bicarb	n	lac/pyr	n	bicarb/pyr	n	lac/pyr	n	bicarb/pyr
2	77.7	30.4	51.6	2.0	12	0.38	12	0.15	8	0.30	8	0.02
3	45.2	18.8	8.7	5.8	20	0.31	20	0.14	0	n/a	0	n/a
4	41.5	11.8	8.5	1.5	7	0.23	7	0.07	0	n/a	0	n/a
5	39.8	10.8	4.0	2.7	13	0.22	13	0.07	0	n/a	0	n/a
6	28.0	9.2	4.4	3.9	10	0.18	10	0.06	0	n/a	0	n/a
7	76.7	28.8	24.8	4.0	16	0.98	16	0.32	2	0.58	2	0.08
8	79.1	34.1	22.8	5.4	20	0.84	20	0.37	5	0.41	5	0.07

Maximum SNR and mean ratios are from voxels that were either: normal appearing brain (NAB)—at least 80% from NAB, not overlapping with the T$_2$ lesion and with lactate SNR >10.0 and bicarbonate SNR > 5.0; or T$_2$ lesion—overlapped by more than 30% with the T$_2$ lesion with lactate SNR >10.0 (n = number of voxels satisfying criteria). Note that the multiband, variable flip angle scheme used for patients 7 and 8 will alter the metabolite ratios. lac, bicarb, and pyr represent lactate, bicarbonate, and pyruvate, respectively.
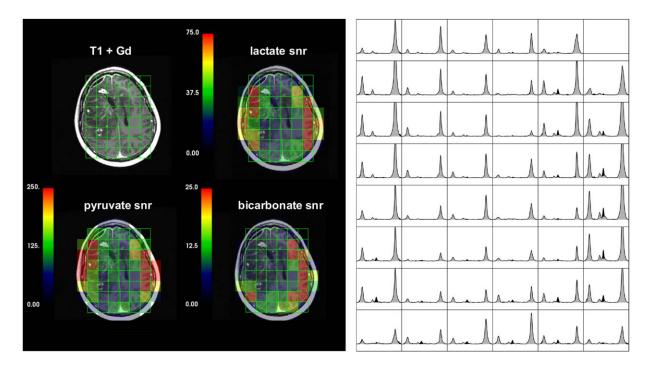n/a, not applicable.

FIG. 6. A post-Gd T_1-weighted image, color maps of integrated pyruvate, lactate, and bicarbonate SNR and arrays of summed spectra from patient 2. The spectra with peaks shaded in gray are from the data reconstructed at the acquired reference frequency, and the peaks shaded in black represent the data reconstructed at the bicarbonate frequency. The lactate and pyruvate peak intensities were determined from the former gray spectra and the bicarbonate peak intensities from the black spectra. The proposed coil setup with the clamshell transmit and the eight-channel bilateral receive arrays allowed the acquisition of ^{13}C signals across the majority of the brain, but with significantly lower SNR in central regions. The low SNR in the center of the brain was accentuated by reduced signal in the ventricles.

ensuing QC procedure, which lasted approximately 37 seconds, extended the time from the start of dissolution to the scan (mean time of 88 seconds) compared to the preclinical system (typically 10–15 seconds), the high polarization levels generated from the SPINlab system were important for providing ^{13}C data from human brain

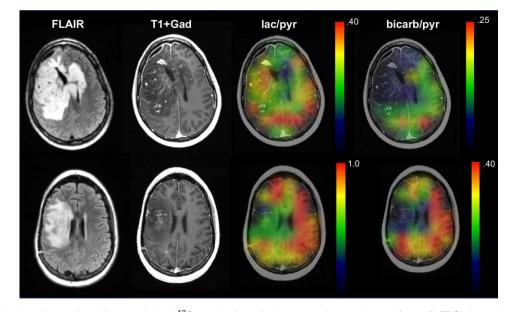FIG. 7. Anatomical and interpolated hyperpolarized ^{13}C metabolite ratio image overlays estimated from 2D EPSI dynamic data acquired at 2 cm in plane resolution and 2-cm slice thickness from 2 patients with treated glioblastoma multiforme. The differences in scales for the color overlay images are attributed to the single-band constant flip angle excitation scheme utilized for patient 2 and the multiband variable flip angle excitation scheme used for patient 8. Note that, in both cases, the bicarbonate/pyruvate was higher in regions of NAB. The patient in the upper images (patient 2) had progressive tumor at the time of this exam, and the patient in the lower images (patient 8) was not characterizing as progressing until subsequent follow-up scans. lac/pyr and bicarb/pyr represent lactate/pyruvate and bicarbonate/pyruvate, respectively.

with high SNR. For patient 3, the pH was measured manually by the pharmacist, which extended the time from dissolution to data acquisition to 114 seconds and resulted in the maximum SNR of pyruvate and lactate being lower compared to other data.

The coil setup with the clamshell transmit and the eight-channel bilateral receive arrays allowed the acquisition of ^{13}C signals across the majority of the brain, but with significantly lower SNR in the central regions. This was expected based upon knowledge of the reception profile of the paddle coils and results from the phantom experiments, but was accentuated by the reduced signal in voxels overlapping the ventricles. Care must be taken when using this experimental setup to avoid the misinterpretation of the variation in the levels of metabolite signals from different parts of the brain. When the SNR is adequate, the use of metabolite ratios provides a more meaningful within-subject comparison. One approach to correct for this is to integrate all of the metabolic signals on a voxel-by-voxel basis for each coil and to use these as estimates of the coil sensitivity maps. Although this provides a simple approach that does not rely upon external standards, it may overestimate parameters in regions with high contributions from the vasculature or when metabolite T_1s are very different. Other methods include the use of coil reception profiles that are estimated from numerical simulations or maps obtained from phantom studies (29), as well as the development of ^{13}C volume or multichannel head coils that provide more homogenous reception profiles.

The time course of signals from the slice-localized and 2D EPSI ^{13}C data showed a similar pattern, with the maximum lactate appearing between 6 and 9 seconds after the maximum pyruvate for all patients. Although there may be differences in the arrival time of the pyruvate based upon heart rate and local vasculature, the values observed for the 2D EPSI data were within one time point of the mean value and were similar to findings from our previously reported studies in nonhuman primates (21). Note that the flip angle excitation scheme employed for patients 2 to 6 was the simplest possible (uniform across the spectrum and constant of $10°$ for each excitation) and the number of phase encodes was similar (10 for patients 2–5, 7, and 8 and 12 for patient 6). Although this does provide a clear picture of the dynamic processes associated with delivery and metabolism of pyruvate within the brain, it uses more of the available magnetization during the early time points than the multiband, variable flip angle scheme used for patients 7 and 8, which began with flip angles of $1.2°$ for pyruvate and $8.7°$ for lactate (22,23). The higher SNR and ratio values that were obtained for lactate and bicarbonate using the more complex acquisition scheme indicates that it should be considered for future studies that require improved spatial resolution and increased coverage. The incorporation of compressed sensing reconstruction (2,30,31) and frequency-specific echo planar imaging (19) are also likely to be important for obtaining 3D ^{13}C metabolic imaging data from the brain.

The bicarbonate signals observed in the patient studies suggest that hyperpolarized ^{13}C pyruvate may be useful for probing mitochondrial metabolism. Although the SNR of bicarbonate peaks was relatively small compared to pyruvate and lactate, it was detected in NAB for 7 of 8 subjects. Of particular interest is that it was clearly present in voxels from contralateral brain, but absent in voxels from the T_2 lesion for patients 2, 7, and 8, whose scans showed sufficiently high enough SNR and had large enough lesions to provide definitive results. This differential is of interest for future studies and needs to be considered in pulse-sequence design. The relatively low metabolite signals in voxels overlapping with the T_2 lesion from patients 3 to 6 are consistent with them either being in regions with low reception profile or corresponding mainly to treatment effects rather than residual or recurrent tumor. None of these voxels were enhancing on corresponding post-Gd T_1-weighted images or were in portions of the lesion that were found to progress in subsequent scans. Although the relatively high conversion of pyruvate to lactate in NAB meant that there was not a clear differential for voxels in the T_2 lesion and surrounding brain for patient 2, who was the only subject with clinical status defined as progressive tumor and had high enough lactate SNR in tumor, it does suggest that this technique may be of interest for studying changes in metabolism associated with other neurological diseases.

The purpose of this paper was to report upon initial patient studies and to introduce the experimental setup that was designed for the acquisition of ^{13}C data from the human brain. Although a relatively small group of patients were included, the time course of changes in metabolite levels and the appearance of lactate and bicarbonate in NAB were consistent between subjects and provide a basis for designing future, more advanced data acquisition schemes and experimental setups. The observation of substantial conversion of pyruvate to lactate in normal brain is in contrast to our previous results in studies from normal rats and nonhuman primates (2,12,21), where the conversion of pyruvate to lactate was relatively low. In our previous rodent studies that used similar experimental conditions, the bicarbonate signal was not detected (12,13); however, there have been several other reports in rats that have demonstrated the detection of bicarbonate in normal brain as well as in glioma (32–34). Whether this was attributed to differences in brain metabolism between humans and other species or because of the anesthesia (35) is unclear. Of interest for evaluating patients with brain tumors is that no bicarbonate was detected in lesions corresponding to recurrent tumor, but that the ratios of lactate/pyruvate in T_2 lesion were similar to or lower than the lactate/pyruvate in NAB. Further technical studies are required to optimize data acquisition parameters for the brain to provide 3D coverage and finer spatial resolution. This will be important for using hyperpolarized ^{13}C agents to characterize metabolism in normal gray and white matter, as well as detecting changes associated with brain tumors and other types of pathology.

CONCLUSIONS

Experimental strategies for implementing hyperpolarized ^{13}C metabolic imaging in the human brain have been developed, and initial patient studies have confirmed

the safety and feasibility of using this technology. The results obtained indicate that hyperpolarized [1-^{13}C]pyruvate was transported across the blood–brain barrier and was converted to metabolic products, [1-^{13}C]lactate and ^{13}C-bicarbonate, in a time frame that can be measured using the pulse sequences and RF coils designed for this study. Although additional optimization is required, these initial findings support further investigation of the technology in patients with brain tumors and other neurological diseases.

ACKNOWLEDGMENTS

REFERENCES

1. Ardenkjaer-Larsen JH, Fridlund B, Gram A, et al. Increase in signal-to-noise ratio of > 10,000 times in liquid-state NMR. Proc Natl Acad Sci U S A 2003;100:10158–10163.
2. Park I, Hu S, Bok R, et al. Evaluation of heterogeneous metabolic profile in an orthotopic human glioblastoma xenograft model using compressed sensing hyperpolarized 3D 13C magnetic resonance spectroscopic imaging. Magn Reson Med 2013;70:33–39.
3. Brindle K. New approaches for imaging tumour responses to treatment. Nat Rev Cancer 2008;8:94–107.
4. Warburg O. On the origin of cancer cells. Science 1956;123:309–314.
5. Albers MJ, Bok R, Chen AP, et al. Hyperpolarized 13C lactate, pyruvate, and alanine: noninvasive biomarkers for prostate cancer detection and grading. Cancer Res 2008;68:8607–8615.
6. DeVience SJ, Lu X, Proctor J, et al. Metabolic imaging of energy metabolism in traumatic brain injury using hyperpolarized [1-13C]pyruvate. Sci Rep 2017;7:1907.
7. Golman K, Petersson JS, Magnusson P, et al. Cardiac metabolism measured noninvasively by hyperpolarized 13C MRI. Magn Reson Med 2008;59:1005–1013.
8. Guglielmetti C, Najac C, Didonna A, Van der Linden A, Ronen SM, Chaumeil MM. Hyperpolarized (13)C MR metabolic imaging can detect neuroinflammation in vivo in a multiple sclerosis murine model. Proc Natl Acad Sci U S A 2017;114:E6982–E6991.
9. Hu S, Balakrishnan A, Bok RA, et al. 13C-pyruvate imaging reveals alterations in glycolysis that precede c-Myc-induced tumor formation and regression. Cell Metab 2011;14:131–142.
10. Kurhanewicz J, Vigneron DB, Brindle K, et al. Analysis of cancer metabolism by imaging hyperpolarized nuclei: prospects for translation to clinical research. Neoplasia 2011;13:81–97.
11. Mignion L, Dutta P, Martinez GV, Foroutan P, Gillies RJ, Jordan BF. Monitoring chemotherapeutic response by hyperpolarized 13C-fumarate MRS and diffusion MRI. Cancer Res 2014;74:686–694.
12. Park I, Larson PE, Zierhut ML, et al. Hyperpolarized 13C magnetic resonance metabolic imaging: application to brain tumors. Neuro-oncology 2010;12:133–144.
13. Park I, Mukherjee J, Ito M, et al. Changes in pyruvate metabolism detected by magnetic resonance imaging are linked to DNA damage and serve as a sensor of temozolomide response in glioblastoma cells. Cancer Res 2014;74:7115–7124.
14. Nelson SJ, Kurhanewicz J, Vigneron DB, et al. Metabolic imaging of patients with prostate cancer using hyperpolarized [1-(1)(3)C]pyruvate. Sci Transl Med 2013;5:198ra108.
15. Cunningham CH, Lau JY, Chen AP, et al. Hyperpolarized 13C Metabolic MRI of the Human Heart: Initial Experience. Circ Res 2016;119:1177–1182.
16. Tropp J, Lupo JM, Chen A, et al. Multi-channel metabolic imaging, with SENSE reconstruction, of hyperpolarized [1-(13)C] pyruvate in a live rat at 3.0 tesla on a clinical MR scanner. J Magn Reson 2011;208:171–177.
17. Ohliger MA, Larson PE, Bok RA, et al. Combined parallel and partial fourier MR reconstruction for accelerated 8-channel hyperpolarized carbon-13 in vivo magnetic resonance Spectroscopic imaging (MRSI). J Magn Reson Imaging 2013;38:701–713.
18. Stollberger R, Wach P. Imaging of the active B$_1$ field in vivo. Magn Reson Med 1996;35:246–251.
19. Gordon JW, Vigneron DB, Larson PE. Development of a symmetric echo planar imaging framework for clinical translation of rapid dynamic hyperpolarized 13 C imaging. Magn Reson Med 2017;77:826–832.
20. Larson PE, Bok R, Kerr AB, et al. Investigation of tumor hyperpolarized [1-13C]-pyruvate dynamics using time-resolved multiband RF excitation echo-planar MRSI. Magn Reson Med 2010;63:582–591.
21. Park I, Larson PE, Tropp JL, et al. Dynamic hyperpolarized carbon-13 MR metabolic imaging of nonhuman primate brain. Magn Reson Med 2014;71:19–25.
22. Larson PE, Hu S, Lustig M, et al. Fast dynamic 3D MR spectroscopic imaging with compressed sensing and multiband excitation pulses for hyperpolarized 13C studies. Magn Reson Med 2011;65:610–619.
23. Xing Y, Reed GD, Pauly JM, Kerr AB, Larson PE. Optimal variable flip angle schemes for dynamic acquisition of exchanging hyperpolarized substrates. J Magn Reson 2013;234:75–81.
24. Crane JC, Olson MP, Nelson SJ. SIVIC: Open-Source, Standards-Based Software for DICOM MR Spectroscopy Workflows. Int J Biomed Imaging 2013;2013:169526.
25. Nelson SJ. Analysis of volume MRI and MR spectroscopic imaging data for the evaluation of patients with brain tumors. Magn Reson Med 2001;46:228–239.
26. Stollberger R, Wach P. Imaging of the active B$_1$ field in vivo. Magn Reson Med 1996;35:246–251.
27. Halestrap AP. Monocarboxylic acid transport. Compr Physiol 2013;3:1611–1643.
28. Ardenkjaer-Larsen JH, Leach AM, Clarke N, Urbahn J, Anderson D, Skloss TW. Dynamic nuclear polarization polarizer for sterile use intent. NMR Biomed 2011;24:927–932.
29. Dominguez-Viqueira W, Geraghty BJ, Lau JY, Robb FJ, Chen AP, Cunningham CH. Intensity correction for multichannel hyperpolarized 13C imaging of the heart. Magn Reson Med 2016;75:859–865.
30. Hu S, Lustig M, Balakrishnan A, et al. 3D compressed sensing for highly accelerated hyperpolarized (13)C MRSI with in vivo applications to transgenic mouse models of cancer. Magn Reson Med 2010;63:312–321.
31. Hu S, Lustig M, Chen AP, et al. Compressed sensing for resolution enhancement of hyperpolarized 13C flyback 3D-MRSI. J Magn Reson 2008;192:258–264.
32. Butt SA, Sogaard LV, Magnusson PO, et al. Imaging cerebral 2-ketoisocaproate metabolism with hyperpolarized (13)C magnetic resonance spectroscopic imaging. J Cereb Blood Flow Metab 2012;32:1508–1514.
33. Park JM, Recht LD, Josan S, et al. Metabolic response of glioma to dichloroacetate measured in vivo by hyperpolarized (13)C magnetic resonance spectroscopic imaging. Neuro-oncology 2013;15:433–441.
34. Park JM, Spielman DM, Josan S, et al. Hyperpolarized (13)C-lactate to (13)C-bicarbonate ratio as a biomarker for monitoring the acute response of anti-vascular endothelial growth factor (anti-VEGF) treatment. NMR Biomed 2016;29:650–659.
35. Josan S, Hurd R, Billingsley K, et al. Effects of isoflurane anesthesia on hyperpolarized (13)C metabolic measurements in rat brain. Magn Reson Med 2013;70:1117–1124.

SUPPORTING INFORMATION

Additional supporting information can be found in the online version of this article.

Fig. S1. Variable flip angle scheme for pyruvate and lactate. The flip angles for bicarbonate were the same as for lactate.